AGU ADVANCING EARTH AND SPACE SCIENCE

JGR Solid Earth

RESEARCH ARTICLE
10.1029/2020JB019740

Key Points:
- Coupled viscoelastic flow and afterslip explain the 8 years of postseismic deformation following the El Mayor-Cucapah earthquake
- The effective viscosity in the lower crust is heterogeneous over space and time
- The mechanical response of the lower crust includes nonlinear transient creep transitioning to steady-state dislocation creep

Supporting Information:
- Supporting Information S1

Correspondence to:
C.-H. Tang,
chihsientang@earth.sinica.edu.tw

Citation:
Tang, C.-H., Barbot, S., Hsu, Y.-J., & Wu, Y.-M. (2020). Heterogeneous power-law flow with transient creep in Southern California following the 2010 El Mayor-Cucapah earthquake. *Journal of Geophysical Research: Solid Earth*, *125*, e2020JB019740. https://doi.org/10.1029/2020JB019740

Received 11 MAR 2020
Accepted 22 AUG 2020
Accepted article online 26 AUG 2020

Heterogeneous Power-Law Flow With Transient Creep in Southern California Following the 2010 El Mayor-Cucapah Earthquake

Chi-Hsien Tang[1,2], Sylvain Barbot[3], Ya-Ju Hsu[1,2], and Yih-Min Wu[1,2,4]

[1]Institute of Earth Sciences, Academia Sinica, Taipei, Taiwan, [2]Department of Geosciences, National Taiwan University, Taipei, Taiwan, [3]Department of Earth Sciences, University of Southern California, Los Angeles, CA, USA, [4]Research Center for Future Earth, National Taiwan University, Taipei, Taiwan

Abstract The rheology of the crust and mantle and the interaction of viscoelastic flow with seismic/aseismic slip on faults control the state of stress in the lithosphere over multiple seismic cycles. The rheological behavior of rocks is well constrained in a laboratory setting, but the *in situ* properties of the lithosphere and its lateral variations remain poorly known. Here, we access the lower-crustal rheology in Southern California by exploiting 8 years of geodetic postseismic deformation following the 2010 El Mayor-Cucapah earthquake. The data illuminate viscoelastic flow in the lower crust with lateral variations of effective viscosity correlated with the geological province. We show that a Burgers assembly with dashpots following a nonlinear constitutive law can approximate the temporal evolution of stress and strain rate, indicating the activation of nonlinear transient creep before steady-state dislocation creep. The transient and background viscosities in the lower crust of the Salton Trough are on the order of ~10^{18} and ~10^{19} Pa s, respectively, about an order of magnitude lower than those in the surrounding regions. We highlight the importance of transient creep, nonlinear flow laws, and lateral variations of rheological properties to capture the entire history of postseismic relaxation following the El Mayor-Cucapah earthquake.

1. Introduction

Large earthquakes are often followed by a transient phase of deformation in the lithosphere associated with the rheological response of crust and mantle rocks to the coseismic stress perturbation. This deformation may be accommodated by various mechanisms, such as pore fluid migration driven by pressure changes (e.g., Hu et al., 2014; Jónsson et al., 2003), aseismic slip (afterslip) surrounding the coseismic rupture along the fault (e.g., Barbot et al., 2009; Hsu et al., 2006), and viscoelastic flow in the ductile lower crust or mantle (e.g., Barbot, 2018a; Freed et al., 2012; Lambert & Barbot, 2016), each causing surface deformation patterns over different spatial and temporal scales. The different sources of deformation can be deconvolved using dense geodetic observatories with long-term observations (e.g., Tang et al., 2019; Weiss et al., 2019). Thus, geodetic measurements following large earthquakes allow us to explore the processes driving the postseismic deformation and to better constrain the rheological properties of the lithosphere.

Southern California is located on the transform boundary of the Pacific and North American plates, where the tectonic setting transitions from the dextral strike-slip faults of the San Andreas Fault system to the oceanic spreading regime of the northern termination of the East Pacific Rise in the Salton Trough. On 4 April 2010, the M_w 7.2 El Mayor-Cucapah (EMC) earthquake ruptured a series of NW-SE-trending strike-slip faults of up to 120 km in the Salton Trough (Fletcher et al., 2014; Hauksson et al., 2011). The earthquake was caused by a predominantly right-lateral slip of up to 6 m along the Sierra Cucapah and Indiviso faults (Wei, Fielding, et al., 2011), causing a stress change of more than 0.1 MPa in the lower crust and notable surface postseismic deformation of up to 5 cm near the rupture area (Figure 1). Postseismic deformation may be associated with localized afterslip, poroelastic rebound, viscoelastic relaxation, or a combination of these processes. Gonzalez-Ortega et al. (2014) analyzed GPS and InSAR data collected over 5 months after the mainshock and suggested that afterslip on the coseismic ruptured fault is the dominant mechanism for the early postseismic deformation. However, the systematic misfits at GPS stations located far from the rupture area imply the potential contribution of viscoelastic flow across large spatial scales. Poroelastic rebound operates in the near-field of the ruptured faults and does not reproduce the long-wavelength deformation

10.1029/2020JB019740

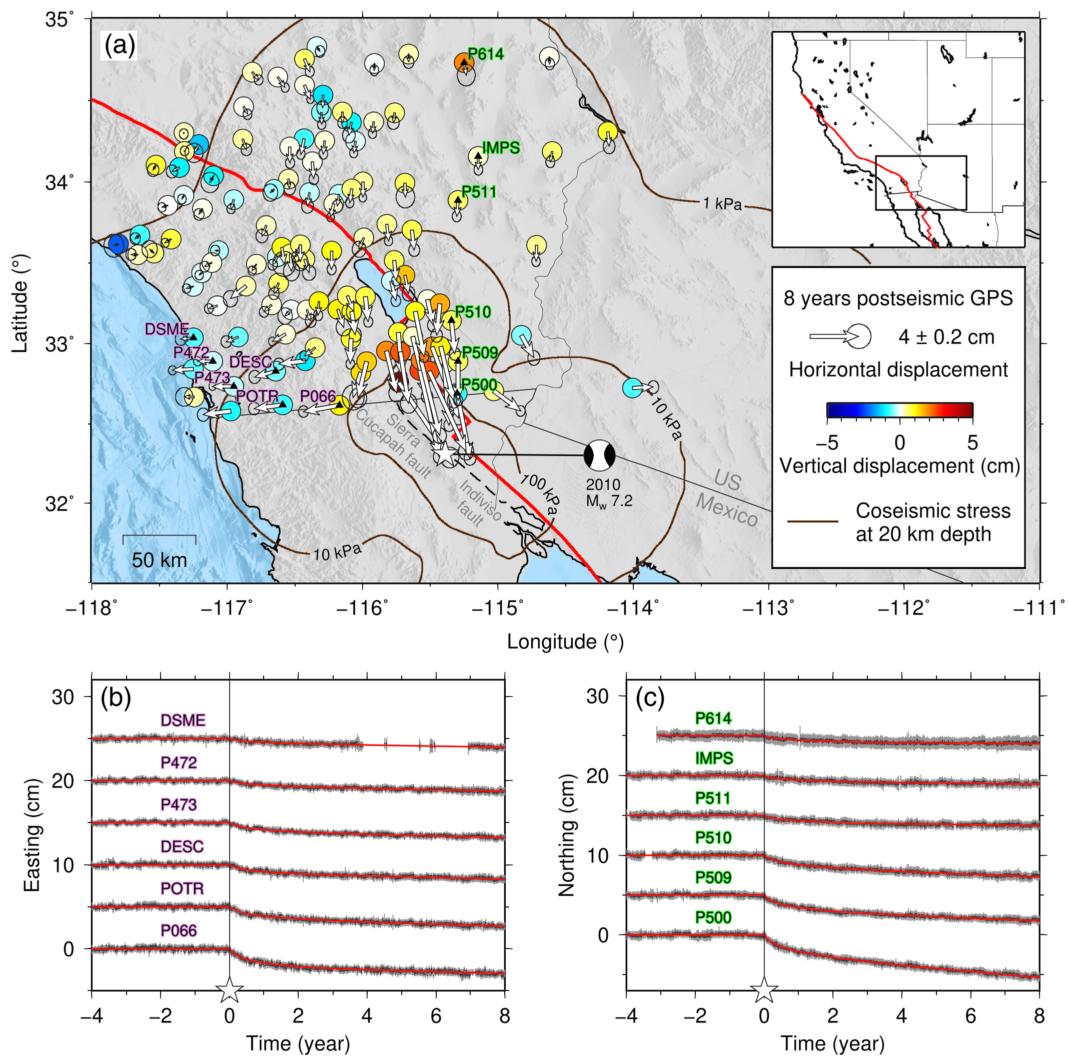

Figure 1. Eight years of postseismic GPS displacements following the 2010 EMC earthquake. (a) Cumulative displacements recorded by PBO GPS network in Southern California. Horizontal and vertical displacements are shown as white vectors and colored circles, respectively. The focal mechanism indicates the EMC mainshock, and the black dashed line represents the surface trace of the coseismic rupture. The brown contours show the deviatoric coseismic stress change at 20 km depth estimated from the coseismic slip model (Wei, Fielding, et al., 2011). Red line illustrates the plate boundary in this region. (b) The east component of corrected GPS time series at the stations with purple-based labels in (a) and (c) the north component at the stations with green-based labels. Coseismic offsets, linear trends, and periodic motions are removed from the time series. Gray bars are the 95% confidence intervals of GPS daily solutions, and red lines are the regression results of each time series. The time axis is with respect to the time of EMC mainshock denoted by the white star.

observed by GPS (Gonzalez-Ortega et al., 2014; Pollitz et al., 2012). Rollins et al. (2015) and Dickinson-Lovell et al. (2018) found that afterslip alone cannot explain far-field GPS postseismic displacements over 3 years, unless with large slip on faults that extend deep into the mantle. As deep afterslip is incompatible with the rheology of the lithosphere, these results may serve as a proxy for distributed viscoelastic flow in the lower crust and/or upper mantle.

The Moho depth in Southern California varies laterally from ~34 km in the Peninsular Ranges, ~22 km in the Salton Trough, to ~26 km in the Mojave Desert and the Basin and Range (Tape et al., 2012) (Figure 2). In the Salton Trough, the shallow Moho (Tape et al., 2012), lithospheric thinning (Lekic et al., 2011), and the high heat flow anomalies (Blackwell & Richards, 2004) imply pronounced lateral rheological heterogeneity in this region. The complex rheological structure may have a profound

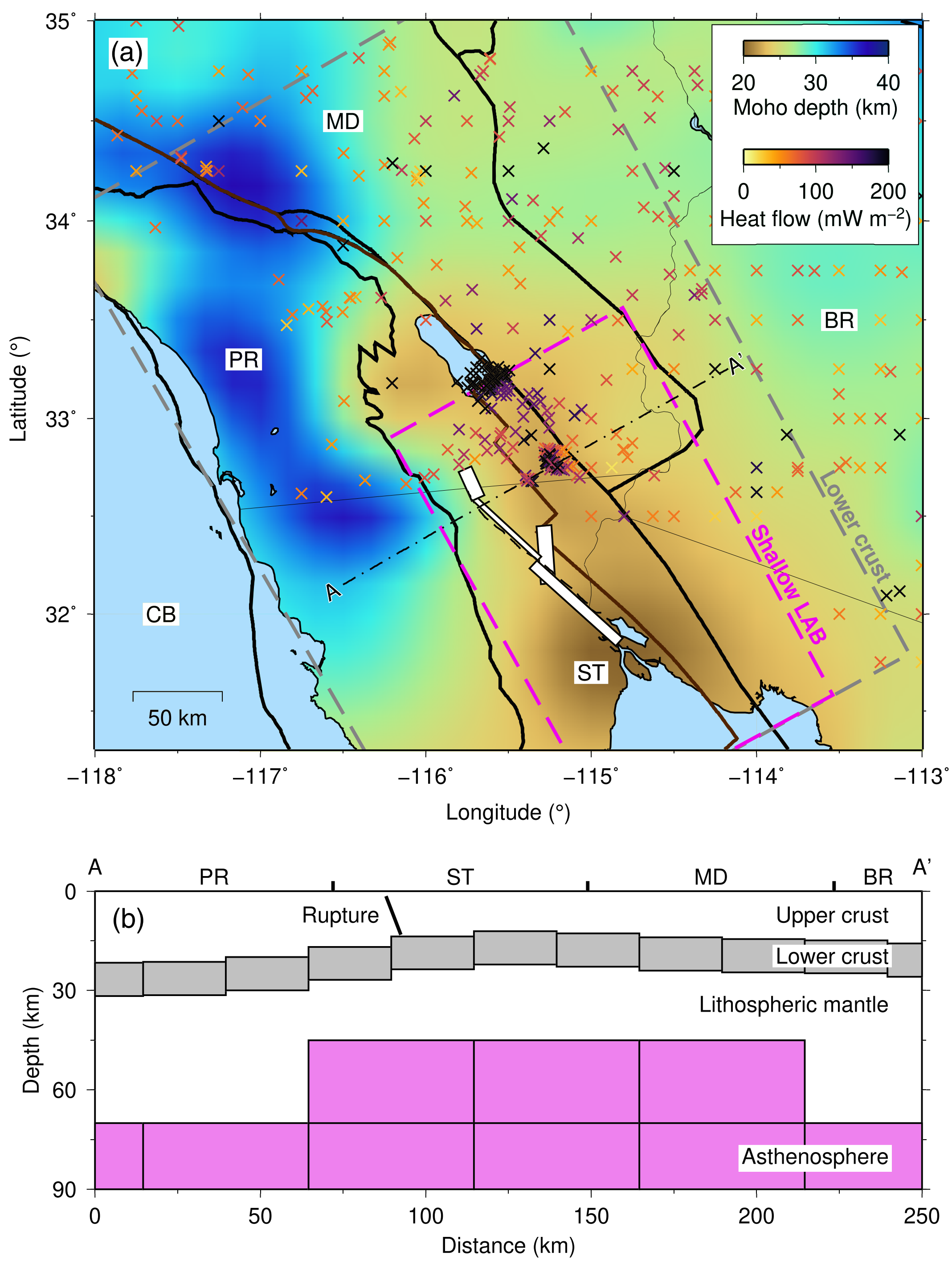

Figure 2. Moho depth (Tape et al., 2012), geological settings (Thatcher et al., 2019), and the 3-D geometry of viscoelastic structure considered in our models. (a) The gray and purple dashed rectangles illustrate the geometry of the weak lower crust and asthenosphere. Black lines are the boundaries of geologic units. Colored crosses mark the observed surface heat flow (Blackwell & Richards, 2004). (b) The lateral variation of the viscoelastic structure along the AA′ cross-section in (a). CB: California Borderland; PR: Peninsular Ranges; ST: Salton Trough; MD: Mojave Desert; BR: Basin and Range.

impact on the pattern of viscoelastic flow. Previous studies of viscoelastic flow in the postseismic phase of the EMC earthquake provided key insights. For instance, Spinler et al. (2015) and Hines and Hetland (2016) propose a layered rheological model with effective viscosities of 10^{19} Pa s for the lower crust and 10^{18} Pa s for the upper mantle. In contrast, Pollitz et al. (2012), Rollins et al. (2015), and Dickinson-Lovell et al. (2018) emphasize the importance of a low-viscosity anomaly in the Salton Trough. Furthermore, Hines and Hetland (2016) argue that a transient rheology describes the postseismic deformation better than a steady-state linear rheology. The disparity of inferred effective viscosities and rheological laws in these studies is due to the different assumptions adopted in forward modeling and the different postseismic periods considered.

Although many sophisticated models with different rheological assumptions can explain some aspects of the postseismic transient following the EMC earthquake, an integrated model is still needed to explain the postseismic geodetic time series. Furthermore, there is a need to identify the *in situ* rheological constitutive laws that govern viscoelastic relaxation in the lithosphere at the time scales of postseismic deformation. To address these issues, we rely on a geodetic inversion method that includes off-fault deformation with volume elements (Barbot, 2018b; Barbot et al., 2017). This approach allows us to treat the whole postseismic deformation problem as a linear kinematic inversion with localized afterslip and distributed anelastic deformation and to constrain the sources of postseismic deformation without prescribing rheology *a priori* (e.g., Moore et al., 2017; Qiu et al., 2018; Tang et al., 2019; Tsang et al., 2016; Weiss et al., 2019). The postseismic deformation of the EMC earthquake is well constrained on the U.S. side by an extensive geodetic network with nearly a decade of continuous records. A remaining challenge is the lack of robust constraints on surface deformation in Mexico. We adapt the inversion method to avoid unrealistic deformation in poorly resolved regions, and we focus our interpretation in Southern California, where the model is better constrained.

We use 8 years of geodetic measurements in the postseismic period of the EMC earthquake to explore the rheological properties of the lithosphere. We will show that the postseismic deformation of the EMC involves viscoelastic flow in the lower crust of Southern California with a low-viscosity zone in the Salton Trough. In addition, we will demonstrate that the constitutive law for lower-crustal flow includes transient and steady-state creep, both characterized by a nonlinear stress/strain-rate relationship. In the next sections, we describe how we isolate the postseismic signal from the geodetic data. We also derive the inversion method used to identify the various mechanisms of postseismic deformation, including afterslip around the coseismic rupture and anelastic strain in the lower crust and asthenosphere. We discuss two end-member models of postseismic deformation by altering the depth extent of the mainshock faults to test the potential tradeoffs between afterslip and viscoelastic flow. Each model provides time series of strain, strain-rate, and stress in the lithosphere that allows us to interrogate the *in situ* rheological behavior. Finally, we adopt two methods to explore the heterogeneous rheological properties in the lower crust over space and time. First, we examine the spatial pattern of effective viscosity with assumed background strain-rate and viscosity. Second, we test how spring-dashpot assemblies may approximate the inferred stress/strain-rate evolution over 8 years. These analyses illuminate the lateral variations of rheological properties in Southern California and identify the constitutive law most suited to explain the geodetic observations. The results provide a refined picture of the lithosphere rheology beneath Southern California.

2. Materials and Methods

2.1. GPS Data Post-Processing

The Plate Boundary Observatory (PBO) GPS network in Southern California provides valuable data to constrain the postseismic deformation following the EMC earthquake. We collect 8 years of postseismic GPS time series data recorded by PBO stations from the Scripps Orbit and Permanent Array Center and the California Spatial Reference Center (SOPAC/CSRC) GPS Archive (http://garner.ucsd.edu/pub/timeseries/measures/ats/WesternNorthAmerica/). The selected PBO stations are located within a 300 km radius of the EMC epicenter (Figure 1a). In each time series, we included observations collected at least 3 years before the EMC mainshock to constrain the secular velocity field. Apart from the 2010 EMC earthquake, the 2010 M_w 5.8 Ocotillo earthquake and the 2012 Brawley swarm, including two $M_w > 5.4$ events, also caused notable coseismic surface displacements at GPS stations used in our study (Hines & Hetland, 2016). To isolate the postseismic transients of the 2010 EMC earthquake, we analyze the GPS time series using a regression with linear trends, annual and semiannual oscillations, coseismic offsets, and postseismic decays, as shown in the following function:

$$x(t) = a + bt + \sum_{n=1}^{2}[p_n \sin(2n\pi t) + q_n \cos(2n\pi t)] + \sum_{i=1}^{N} h_i H(t - T_i) + \sum_{j=1}^{2} b_j H(t - T_{\mathrm{EMC}}) B\left(t - T_{\mathrm{EMC}}, \tau_j, k_j\right) \tag{1}$$

where $x(t)$ is the three-dimensional (east, north, and vertical components) position at time t; a is a constant; b is the secular velocity; p_n and q_n, $n \in \{1, 2\}$, represent for the amplitudes of annual and semiannual motions; h_i is the static offset followed by a Heaviside step function H at epoch T_i; b_j is the amplitude of the postseismic deformation following the time of the EMC earthquake T_{EMC} with the temporal basis function B given by

$$B(t,\, \tau,\, k) = 1 - \frac{2}{k}\coth^{-1}\left[e^{\left(\frac{t}{\tau}\right)}\coth\left(\frac{k}{2}\right)\right] \tag{2}$$

where τ is the characteristic time of the postseismic deformation; k is the dimensionless ratio controlling the nonlinearity of transient deformation (Barbot et al., 2009). In the case of $k \to 0$, equation 2 converges to

$$B(t, \tau, k \to 0) = 1 - e^{\left(-\frac{t}{\tau}\right)} \tag{3}$$

that is, the exponential decay.

We fit all the GPS time series at different stations with two unified sets of temporal basis functions. We carry out a grid search within the given ranges to determine the parameters of two basis functions that minimize the data misfit. For the first temporal basis function, the given ranges for τ and k are from 1 to 10 years and from 1 to 7, respectively, with the search intervals of 1 year and 1. For the second basis function, we allow a wider range of τ from 10 to 50 years, with the search interval of 10 years, and $k = 0$. As a result, the parameters are $\tau = 1$ year and $k = 3$ and $\tau = 50$ year and $k = 0$ for the first and second temporal basis functions, respectively. We eliminate data outliers with residuals larger than three times the root-mean square deviation in each GPS position time series after the first regression. Then, we do the regression again to refine all the linear model parameters in equation 1. We isolate the postseismic deformation signals associated with the EMC earthquake by removing all the other terms estimated from the regression (Figure 1b).

2.2. Postseismic Deformation Modeling

We design a kinematic joint inversion to image localized afterslip on the faults and distributed viscoelastic strain accruing in the lower crust and asthenosphere following the EMC earthquake. The observed surface displacements are related to slip on faults and anelastic strain within subsurface volume elements by

$$\boldsymbol{d} = \boldsymbol{G}\widehat{\boldsymbol{m}} + \boldsymbol{\varepsilon} \tag{4}$$

where $\boldsymbol{G}$ is a matrix that relates data vector $\boldsymbol{d}$ to a model vector $\widehat{\boldsymbol{m}}$, while $\boldsymbol{\varepsilon}$ is a residual vector. The matrix $\boldsymbol{G}$ is given by

$$\boldsymbol{G} = \left[\boldsymbol{G}_{\mathrm{slip}} | \boldsymbol{G}_{\mathrm{strain}}\right] = \left[\boldsymbol{G}_{\mathrm{s}} \;\; \boldsymbol{G}_{\mathrm{d}} | \; \boldsymbol{G}_{11} \quad \boldsymbol{G}_{12} \quad \boldsymbol{G}_{13} \quad \boldsymbol{G}_{22} \quad \boldsymbol{G}_{23} \quad \boldsymbol{G}_{33}\right] \tag{5}$$

where $\boldsymbol{G}_{\mathrm{slip}}$, formed by $\boldsymbol{G}_{\mathrm{s}}$ and $\boldsymbol{G}_{\mathrm{d}}$, and $\boldsymbol{G}_{\mathrm{strain}}$, formed by $\boldsymbol{G}_{11}$, $\boldsymbol{G}_{12}$, $\boldsymbol{G}_{13}$, $\boldsymbol{G}_{22}$, $\boldsymbol{G}_{23}$, and $\boldsymbol{G}_{33}$, relate surface displacements to fault slip (Okada, 1985) and anelastic strain (Barbot et al., 2017), respectively. The corresponding model vector $\widehat{\boldsymbol{m}}$ is

$$\widehat{\boldsymbol{m}} = \left[\frac{\widehat{\boldsymbol{m}}_{\text{slip}}}{\widehat{\boldsymbol{m}}_{\text{strain}}}\right] = \begin{bmatrix} \widehat{\boldsymbol{m}}_{\text{s}} \\ \widehat{\boldsymbol{m}}_{\text{d}} \\ \hline \widehat{\boldsymbol{m}}_{11} \\ \widehat{\boldsymbol{m}}_{12} \\ \widehat{\boldsymbol{m}}_{13} \\ \widehat{\boldsymbol{m}}_{22} \\ \widehat{\boldsymbol{m}}_{23} \\ \widehat{\boldsymbol{m}}_{33} \end{bmatrix} \tag{6}$$

where $\widehat{\boldsymbol{m}}_{\text{slip}}$, formed by $\widehat{\boldsymbol{m}}_{\text{s}}$ and $\widehat{\boldsymbol{m}}_{\text{d}}$, are the strike- and dip-slip on fault patches, while $\widehat{\boldsymbol{m}}_{\text{strain}}$, formed by $\widehat{\boldsymbol{m}}_{11}$, $\widehat{\boldsymbol{m}}_{12}$, $\widehat{\boldsymbol{m}}_{13}$, $\widehat{\boldsymbol{m}}_{22}$, $\widehat{\boldsymbol{m}}_{23}$, and $\widehat{\boldsymbol{m}}_{33}$, represents the six components of the anelastic strain in volume elements.

We add a smoothing constraint on the slip distribution by minimizing the shear stress changes associated with afterslip on the fault by

$$\lambda_1 \boldsymbol{K}\hat{\boldsymbol{m}}_{\text{slip}} = \lambda_1 \begin{bmatrix} \boldsymbol{K}_{\text{ss}} & \boldsymbol{K}_{\text{ds}} \\ \boldsymbol{K}_{\text{sd}} & \boldsymbol{K}_{\text{dd}} \end{bmatrix} \begin{bmatrix} \hat{\boldsymbol{m}}_{\text{s}} \\ \hat{\boldsymbol{m}}_{\text{d}} \end{bmatrix} = \boldsymbol{0} \tag{7}$$

where $\boldsymbol{K}_{ij}$, $i,j \in \{s,d\}$, are the kernels relate shear stress change in the component j due to the afterslip in the component i, with s and d indicating the components of strike and dip, respectively (Okada, 1992). The parameter λ_1 controls the weight of the constraint, which enforces a smooth distribution of afterslip. Also, we penalize afterslip on the fault patches that experience large coseismic slip during the mainshock by

$$\lambda_2 \boldsymbol{P}\hat{\boldsymbol{m}}_{\text{slip}} = \lambda_2 \begin{bmatrix} \boldsymbol{K}_{\text{p}} & \boldsymbol{0} \\ \boldsymbol{0} & \boldsymbol{K}_{\text{p}} \end{bmatrix} \begin{bmatrix} \hat{\boldsymbol{m}}_{\text{s}} \\ \hat{\boldsymbol{m}}_{\text{d}} \end{bmatrix} = \boldsymbol{0} \tag{8}$$

where $\boldsymbol{K}_{\text{p}}$ is a diagonal matrix containing the coseismic shear stress change, when negative, and zeros otherwise. Hence, there is no penalization of afterslip on patches with positive coseismic stress change. The values of coseismic shear stress are projected along the rake of 180°, and the absolute value is used to form the matrix $\boldsymbol{K}_{\text{p}}$. The parameter λ_2 is the weight of the constraint. The combination of equations 7 and 8 allows a smooth distribution of afterslip surrounding the coseismic slip in the inverse model.

Due to the asymmetric distribution of GPS stations, it is challenging to examine the deformation to the south of the U.S.-Mexico border. To tackle the non-uniqueness issue and avoid unrealistic deformation, we regularize the inversion with another constraint assuming that viscoelastic flow in the lower crust and asthenosphere tends to relax a fraction of the deviatoric coseismic stress change in each volume element, following

$$\lambda_3 \boldsymbol{L}\widehat{\boldsymbol{m}}_{\text{strain}} = \lambda_3 \begin{bmatrix} \boldsymbol{L}_{1111} & \boldsymbol{L}_{1211} & \boldsymbol{L}_{1311} & \boldsymbol{L}_{2211} & \boldsymbol{L}_{2311} & \boldsymbol{L}_{3311} \\ \boldsymbol{L}_{1112} & \boldsymbol{L}_{1212} & \boldsymbol{L}_{1312} & \boldsymbol{L}_{2212} & \boldsymbol{L}_{2312} & \boldsymbol{L}_{3312} \\ \boldsymbol{L}_{1113} & \boldsymbol{L}_{1213} & \boldsymbol{L}_{1313} & \boldsymbol{L}_{2213} & \boldsymbol{L}_{2313} & \boldsymbol{L}_{3313} \\ \boldsymbol{L}_{1122} & \boldsymbol{L}_{1222} & \boldsymbol{L}_{1322} & \boldsymbol{L}_{2222} & \boldsymbol{L}_{2322} & \boldsymbol{L}_{3322} \\ \boldsymbol{L}_{1123} & \boldsymbol{L}_{1223} & \boldsymbol{L}_{1323} & \boldsymbol{L}_{2223} & \boldsymbol{L}_{2323} & \boldsymbol{L}_{3323} \\ \boldsymbol{L}_{1133} & \boldsymbol{L}_{1233} & \boldsymbol{L}_{1333} & \boldsymbol{L}_{2233} & \boldsymbol{L}_{2333} & \boldsymbol{L}_{3333} \end{bmatrix} \begin{bmatrix} \widehat{\boldsymbol{m}}_{11} \\ \widehat{\boldsymbol{m}}_{12} \\ \widehat{\boldsymbol{m}}_{13} \\ \widehat{\boldsymbol{m}}_{22} \\ \widehat{\boldsymbol{m}}_{23} \\ \widehat{\boldsymbol{m}}_{33} \end{bmatrix} = -\lambda_3 \phi \Delta\tau_0 \tag{9}$$

where $\boldsymbol{L}_{kl}$, k, $l \in \{11, 12, 13, 22, 23, 33\}$, are the kernels relate stress change in the component l at the center of each volume element due to the anelastic strain in the component k (Barbot et al., 2017). The coseismic stress change $\Delta\tau_0$ at the center of each volume element is estimated by the slip model from Wei, Fielding, et al. (2011). The unknown release ratio of stress ϕ ranging from 0 to 1 indicates "no release" and "full release" of stress, respectively, is time-dependent, and is obtained by solving an optimization problem. The parameter λ_3 is the overall weight of this constraint. Although this regularization may confine the pattern of anelastic strain plausibly, it does not indicate that we can resolve the distributed deformation in the areas with few observations. Finally, we assume that viscoelastic flow is deviatoric. Therefore, we penalize isotropic strain by using

$$\lambda_4 \boldsymbol{Q}\widehat{\boldsymbol{m}}_{\text{strain}} = \lambda_4[\boldsymbol{I} \quad \boldsymbol{0} \quad \boldsymbol{0} \quad \boldsymbol{I} \quad \boldsymbol{0} \quad \boldsymbol{I}]\begin{bmatrix} \widehat{\boldsymbol{m}}_{11} \\ \widehat{\boldsymbol{m}}_{12} \\ \widehat{\boldsymbol{m}}_{13} \\ \widehat{\boldsymbol{m}}_{22} \\ \widehat{\boldsymbol{m}}_{23} \\ \widehat{\boldsymbol{m}}_{33} \end{bmatrix} = \boldsymbol{0} \tag{10}$$

where $\boldsymbol{I}$ is the identity matrix with its size equivalent to the number of volume elements and λ_4 is the weight of the constraint.

To conduct the inversion, we formulate the new data vector $\boldsymbol{h}$ as a function of ϕ.

$$\boldsymbol{h}(\phi) = \begin{bmatrix} \boldsymbol{d} \\ \boldsymbol{0} \\ \boldsymbol{0} \\ -\lambda_3\phi\Delta\tau_0 \\ \boldsymbol{0} \end{bmatrix} \tag{11}$$

and the associated matrix $\boldsymbol{H}$

$$\boldsymbol{H} = \begin{bmatrix} \boldsymbol{G}_{\text{slip}} & \boldsymbol{G}_{\text{strain}} \\ \lambda_1\boldsymbol{K} & \boldsymbol{0} \\ \lambda_2\boldsymbol{P} & \boldsymbol{0} \\ \boldsymbol{0} & \lambda_3\boldsymbol{L} \\ \boldsymbol{0} & \lambda_4\boldsymbol{Q} \end{bmatrix} \tag{12}$$

We allow the different ϕ in the lower crust and asthenosphere, and we search the optimal values by solving a multivariable optimization problem to minimize the norm of residuals given by

$$\hat{\phi} = \min_{\phi}\left\| \boldsymbol{d} - \boldsymbol{G}\left[\left(\boldsymbol{H}^T\boldsymbol{H}\right)^{-1}\boldsymbol{H}^T\boldsymbol{h}(\phi)\right]\right\|_2 \tag{13}$$

with a bound constraint of $0 < \phi < 1$. The corresponding model vector is

$$\hat{\boldsymbol{m}} = \left(\boldsymbol{H}^T\boldsymbol{H}\right)^{-1}\boldsymbol{H}^T\boldsymbol{h}\left(\hat{\phi}\right) \tag{14}$$

We treat the first, third, and sixth months and annual (from first to eighth year) cumulative GPS postseismic displacements as our data in the joint inversion. The inversions at different epochs are carried out independently.

The geometry of our models is illustrated in Figure 2. The surface deformation can be associated with localized faulting in the brittle crust and/or distributed anelastic strain in the ductile regions (e.g., Barbot, 2018b; Barbot & Fialko, 2010). We mesh the weak lower crust with 25-km by 25-km by 10-km volume elements overlying the strong lithospheric mantle. We align the strike of the volume elements with the average strike of the geological structure (~N30°W) and match their bottom surface with the Moho depth (Tape et al., 2012). The prominent lateral variation of Moho depth in the study area allows anelastic strain with a depth ranging from ~12 to ~36 km. The shallow brittle-ductile transition ranging from 12 to 16 km in the Salton Trough is consistent with the high heat flow anomalies (>150 mW/m^2; Blackwell & Richards, 2004) in this area (Figure 2b). The geothermal gradient can yield up to 45°C/km assuming a thermal conductivity of 3.3 W/m^2/K, which is the upper bound value for granites (Lillie, 1999), indicating that the temperature at a depth of 12 km may exceed 500°C. Such a high temperature can also be evaluated by the shallow Curie point depth in the same region (580°C from 8 to 12 km depth), although the estimation may vary with the spatial sampling rate of the magnetic data (Mickus & Hussein, 2016). In addition, we allow viscoelastic flow in the asthenosphere. We approximate the geometry of the lithosphere-asthenosphere boundary (LAB) depth variations, which is derived from the Sp receiver functions (Lekic et al., 2011), with 50-km by 50-km by 25-km volume elements. The LAB in the Salton Trough is at a depth of 45 km and deepens to 70 km at the periphery of the trough. The bottom of the asthenosphere in our model is at a depth of 120 km. For afterslip modeling, we use the fault geometry for the EMC earthquake proposed by Wei, Fielding, et al. (2011) and divide the fault into 3-km by 3-km square patches. For afterslip, we consider two models, one with afterslip extending to a depth of about 13 km, with the bottom of the fault touching the top of the weak lower crust in the Salton Trough (Figure 2b) and another where a shear zone extends into the lower crust, with afterslip possibly extending to the Moho.

3. Results

3.1. GPS Postseismic Displacement Field

We show the signature of 8-year GPS postseismic transients following the EMC mainshock in Figure 1. The regression results show that the given two sets of basis functions can capture the primary features of early and prolonged postseismic deformation simultaneously over an 8-year period (Figure 1b). In the Peninsular Ranges, the postseismic transient exhibits a westward movement and slight subsidence. To the north of the mainshock, the records show a southward movement and a broad uplift. The amplitudes of GPS postseismic displacements decrease with distance from the epicenter, roughly correlated with the magnitude of the coseismic stress perturbation field (Figure 1a). In the Salton Trough, we observe notable postseismic decays, which can be either contributed by localized afterslip or viscoelastic flow related to transient rheology. Furthermore, we found postseismic decay at the far-field GPS stations located at a distance greater than 250 km from the mainshock, implying the presence of deep viscoelastic flow over the postseismic period (Figure 1).

3.2. Inverted Afterslip and Viscoelastic Flow

We first consider a model where afterslip is only allowed down to ~13 km. An alternative model with deeper afterslip is discussed in section 4.2 and supporting information. The shallow afterslip model shows ~1 m of afterslip on the northern segments of the coseismic rupture over 8 years of postseismic period. On the northernmost segment (Figure 3, fault segment 1), afterslip concentrates close to the surface. On the Sierra Cucapah fault (Figure 3, fault segment 2), a deep-seated afterslip occurs on the downdip edge of large coseismic slip, similar to the slip distribution proposed by Gonzalez-Ortega et al. (2014). Afterslip causes significant horizontal surface displacements from the near field to the Salton Sea (Figures 3a and 4a), with uplift of up to 40 mm to the north of the faults and subsidence of ~1 mm in the Peninsular Ranges (Figure 5a). The estimated geodetic moment released by afterslip is equivalent to an earthquake with M_w 6.7, about 20% of the seismic moment released by the EMC mainshock. The postseismic geodetic moment is also greater than the cumulative moment release of M_w 6.3 for the aftershocks that occurred over the same period. Afterslip contributes 30–50% of surface deformation at the GPS stations close to the fault zone, while another 50–70% is due to viscoelastic flow (Figure 3a).

The distributed viscoelastic flow in the lower crust roughly follows the contours of Moho depth, with a large amount of strain beneath the Salton Trough (Figure 4). The inferred internal strain is equivalent to an ~15% reduction of coseismic stress changes in the lower crust and ~50% in the asthenosphere over 8 years. The viscoelastic flow in the lower crust produces a large amount of horizontal motion in the Salton Trough, roughly parallel to the coseismic rupture, with subsidence of 1–2 mm surrounding this region. (Figure 5b). In the asthenosphere, the inverted strain is less than 1 microstrain (Figure 4b), but it causes the broad uplift of ~10 mm from the Salton Trough to further north, along with the eastward surface displacements in the Peninsular Ranges (Figure 5c).

The combination of afterslip and viscoelastic flow can explain the postseismic deformation following the EMC earthquake. Although part of the residuals may be due to triggered slip on distant faults excluded in our model (Wei, Sandwell, et al., 2011), we can capture the primary spatial features of horizontal and vertical GPS postseismic displacements (Figures 5d–5f). The model can also provide a satisfactory fit to the postseismic GPS time series over 8 years with a variance reduction of ~90% for the entire data set (Figure 6).

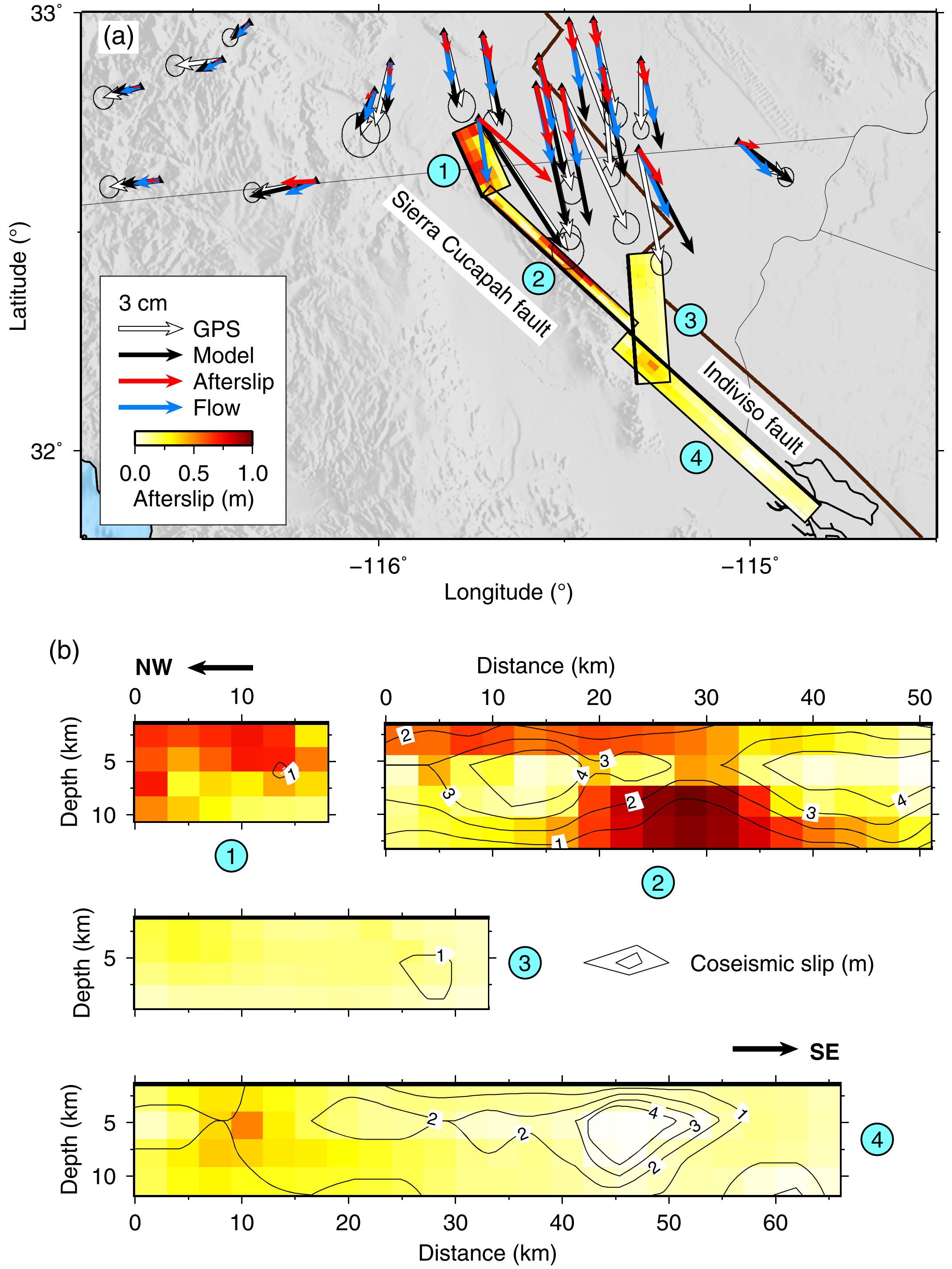

Figure 3. Inferred cumulative afterslip over 8 years on the faults. (a) Map view of the afterslip distributions on four fault segments. The top of each fault segment is marked by thick black lines. Observed and predicted GPS horizontal displacements are shown in white and black vectors, respectively. Contributions of afterslip and viscoelastic flow are in red and cyan vectors, respectively. (b) Side-projected depth profiles of afterslip on four fault segments. The profiles are shown along NW-SE direction from left to right. Contours show the coseismic slip distribution estimated by Wei, Fielding, et al. (2011).

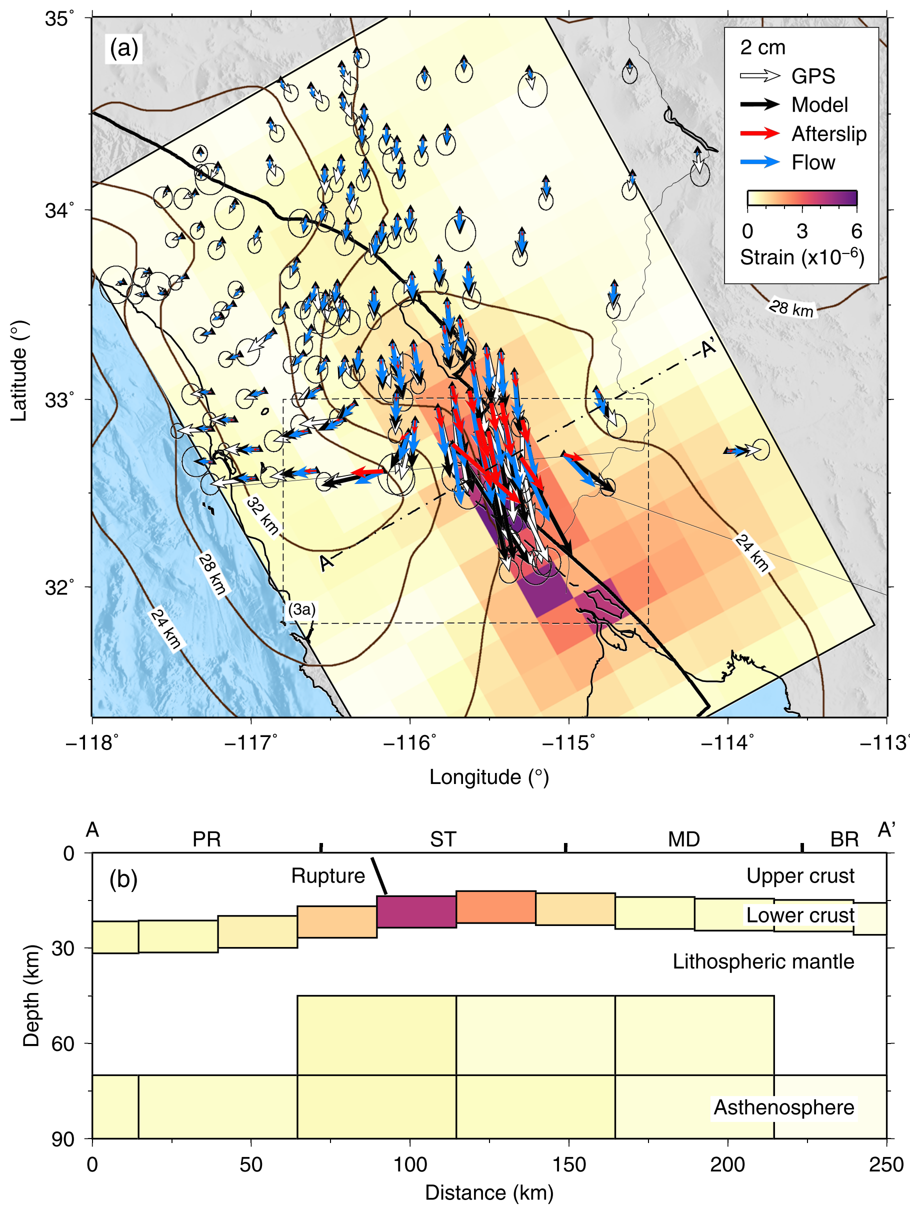

Figure 4. Inferred cumulative viscoelastic flow in the lower crust and asthenosphere over 8 years. (a) Map view of the viscoelastic flow in the lower crust. The viscoelastic strain is indicated as the second invariant of the strain tensor. White and black vectors indicate observations and predictions of horizontal displacements, respectively. Red and cyan vectors are modeled displacements due to afterslip and viscoelastic flow, respectively. Brown contours are the Moho depths as shown in Figure 2a. The black dashed box marks the extent of Figure 3a. (b) The depth profile for viscoelastic flow along the AA′ cross-section in (a).

4. Discussion

4.1. Resolving Power of the PBO GPS Network

The dense GPS array used in our study only spans the northern region of the EMC coseismic rupture. This configuration implies that the model resolution is insufficient to the south of the rupture. To evaluate the resolving power of the PBO GPS network for afterslip, we use a proxy by summing up the magnitude of three-dimensional displacements on all GPS stations caused by unit slip on each fault element (Loveless & Meade, 2011). We add up the resolving power for strike- and dip-slip motions and normalize these values (Figure S1a). We obtain the highest spatial resolution in the northwestern segment of the Sierra Cucapah

10.1029/2020JB019740

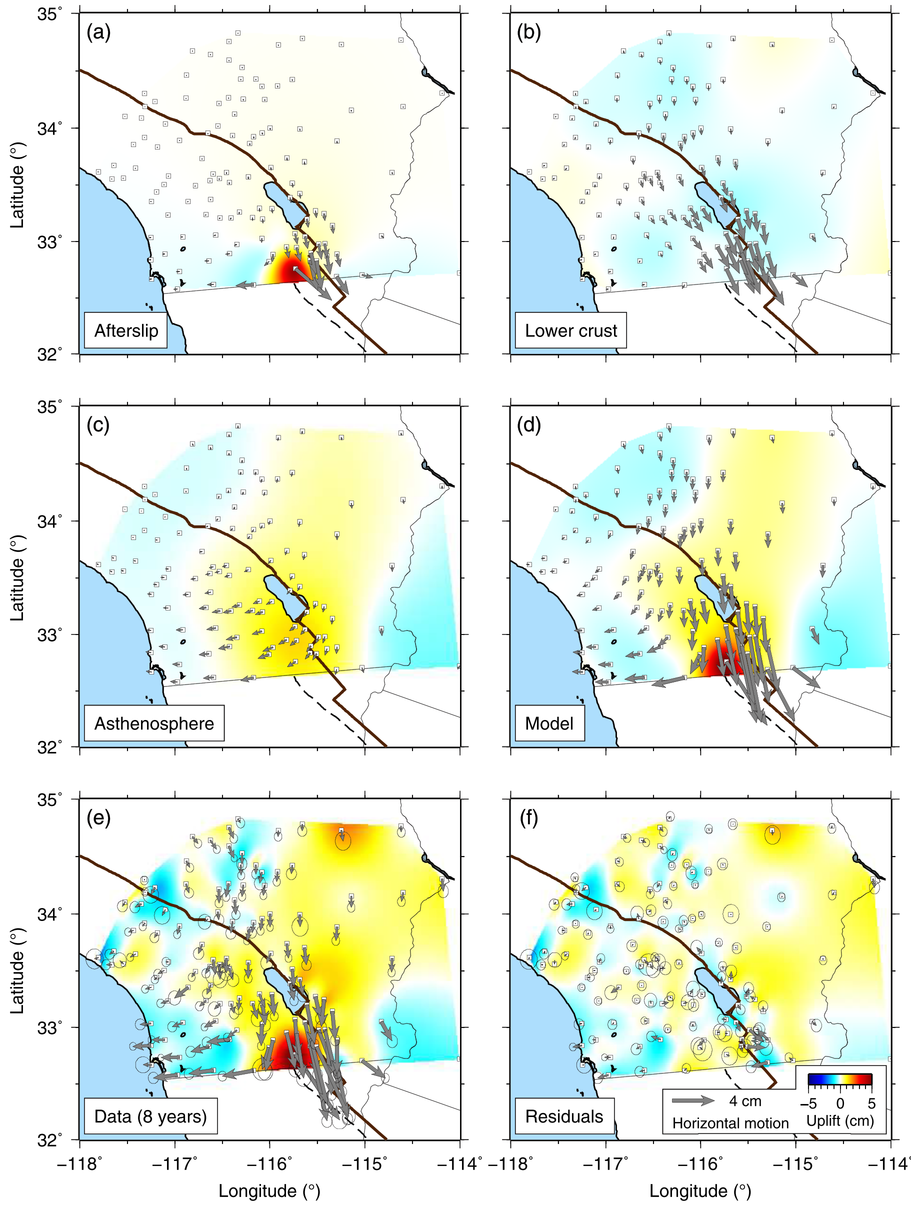

Figure 5. Observed and modeled 8-year cumulative GPS postseismic displacements. Horizontal and vertical surface displacements are indicated by gray vectors and background colors, respectively. (a) Afterslip; (b) lower-crustal flow; (c) asthenosphere relaxation; (d) total modeled deformation; (e) observations; (f) residuals.

fault, greatly decreasing southeastward. The lowest spatial resolution occurs on the southeastern tip of the Indiviso fault, where geodetic constraints are absent. The relatively high resolving power for the Sierra Cucapah fault includes the area where our model images a large amount of afterslip, while only little slip is inferred on the Indiviso fault (Figure 3). More geodetic data are required to constrain the slip behavior on the Indiviso fault.

We employ the same approach to compute the resolving power of the GPS array for viscoelastic strain in each lower-crustal volume element. Similar to afterslip, we normalize the sum of the resolving power on six strain components for each volume element in the lower crust (Figure S1b). Due to the dense GPS coverage, the volume elements beneath Southern California have a relatively high resolving power, especially in the northern tip of the Salton Trough. In Baja California, the resolving power for the lower crust is unsatisfactory, indicating that the imaged viscoelastic flow in this area results from the constraint of coseismic stress

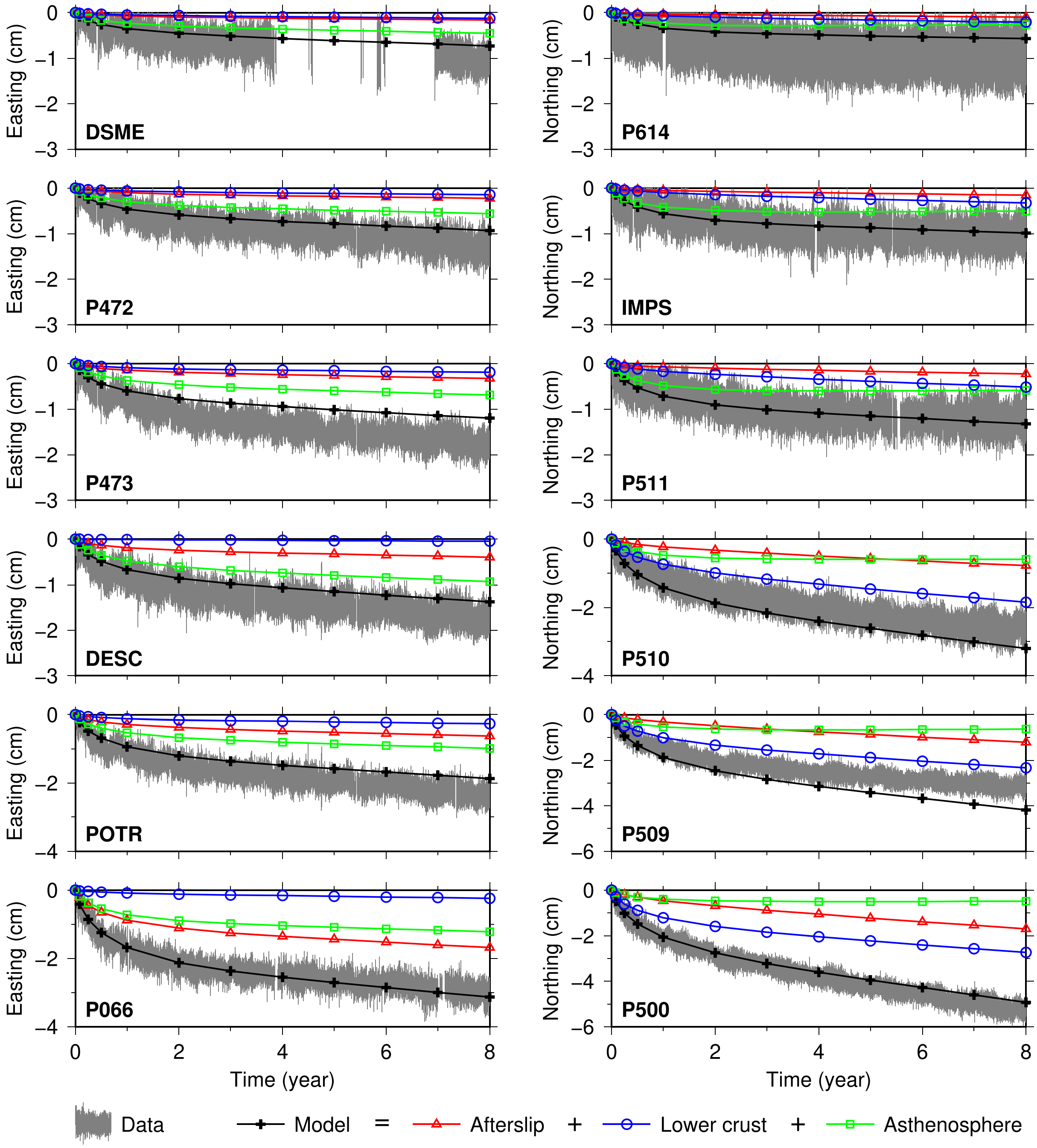

Figure 6. The fits of different model components to the GPS time series at sampled stations (shown in Figure 1). The time series on the left panels refer to Figure 1b and the right panels are to Figure 1c. GPS daily solutions with 95% confidence intervals are indicated by gray bars. Black lines show the interval deformation sampled at two epochs (black crosses), which is equivalent to the sum of contributions from afterslip (red triangles), lower crust (blue circles), and asthenosphere (green squares). Note the changes in *y*-axis limits.

release. Although the estimated resolving power of the GPS array gives us an idea of the relative resolution of each model element, it cannot determine the trade-offs between afterslip and viscoelastic strain. We discuss this issue further with a series of synthetic tests in section 4.3.

4.2. The Possibility of Deep Afterslip in the Lower Crust

Modeling of geodetic data during the seismic cycle is often plagued by epistemic uncertainties related to assumptions about the location and extent of faults. To discuss and mitigate such potential bias, we compare two end-member models of postseismic deformation that either include or exclude afterslip in the lower-crustal extension of the mainshock faults. The modeling assumptions for the "shallow-fault" model are described in section 3.2, and the corresponding results are shown in Figures 3–6. For the "deep-fault" model, we conduct another inversion with the same data set, but we extend the Sierra Cucapah-Indiviso fault system down to the Moho (Figures S2–S5). With this assumed geometry, the deep-fault model produces afterslip down to greater depths (Figure S2, fault segment 2), with slightly less afterslip on the northernmost fault segment (Figure S2, fault segment 1) and more afterslip on the Indiviso fault (Figure S2, fault segment 4). Below the rupture, the 8 years of viscoelastic flow is reduced in the lower crust and increased in the asthenosphere (Figure S3), corresponding to ~8% and ~100% reduction of coseismic stress changes, respectively. In the asthenosphere, the large discrepancy of stress release ratio between two end-member models is likely due to a relatively low coseismic stress change, implying limited constraints on rheological properties.

Despite the different inferred distributions of afterslip and viscoelastic flow, these models can fit the observed GPS postseismic time series equally well (Figures S4 and S5), underscoring the inevitable trade-offs between various postseismic mechanisms when only sparse observations are available (e.g., Bruhat et al., 2011). As the geodetic observatory south of the international border is insufficient for model selection, we consider both modeling results in the following parts of the discussion, and we narrow our conclusions to the set that is compatible with both assumptions.

4.3. Trade-Offs Between Afterslip and Viscoelastic Flow

We test the trade-offs between afterslip and viscoelastic flow with the adopted GPS array from a series of synthetic tests (Figures S6–S10). We construct the initial models by considering four scenarios, including (1) the shallow-fault model with a viscoelastic flow corresponding to a 20% coseismic stress release and no afterslip; (2) the shallow-fault model with 1 m of afterslip surrounding the coseismic slip and no viscoelastic flow; (3) the deep-fault model with a viscoelastic flow corresponding to a 20% coseismic stress release and no afterslip; and (4) the deep-fault model with 1 m of afterslip surrounding the coseismic slip and no viscoelastic flow. For Tests 2 and 4, the initial right-lateral afterslip occupies the selected patches that experience positive coseismic shear stress change along the rake of 180° in the Sierra Cucapah-Indiviso fault system (Figures S7 and S9, fault segments 1, 2, and 4). We compute synthetic surface displacements at each GPS station and then invert for afterslip and viscoelastic flow following equations 13 and 14 with the same constraints and penalizations as for the observations.

We focus on the trade-offs between afterslip and lower-crustal flow due to the limited constraints on the deformation in the asthenosphere. In Test 1, although the recovered model only resolves a small amount of afterslip, the model cannot fully recover the viscoelastic flow in the lower crust (Figure S6). This is due to the asymmetric data distribution and a lack of data near the faults in Baja California, where the largest deformation occurs (Figure S10). This shows that although we impose the constraint on the released stress ratio, a denser station coverage is still needed to constrain the deformation in the fault zone. In Test 2, the model recovers the afterslip on the fault segment 1, but the smearing on the fault segments 2 and 4 is significant (Figure S7). Although the recovery of afterslip distribution is limited, the model only resolves a little viscoelastic flow in the lower crust (Figure S10). In Test 3, similar trade-offs between afterslip and viscoelastic flow are found, while the magnitude of lower-crustal flow is further suppressed due to afterslip at the same depth (Figures S8 and S10). In Test 4, the magnitude of resolved viscoelastic strain beneath the fault zone is similar to Test 2, while the recovery of afterslip on the fault segment 2 improves (Figures S9 and S10). These synthetic tests demonstrate that resolving afterslip and viscoelastic flow beneath the fault zone is challenging. However, the recovery of the model improves significantly as the density of GPS stations increases to the north (Figure S10). We therefore focus the analysis on the deformation that occurs north of the international border, where the GPS station density constrains the deformation well. Since the depth of afterslip cannot be well constrained with the data available, we limit our conclusions to those that apply in both end-member models.

4.4. Lateral Variation of Lower-Crustal Transient Viscosity

We use the inverted viscoelastic flow in the lower crust to examine the lateral variation of transient viscosity. The viscosity of rocks is controlled by complex interactions among multiple rheological parameters, including stress level, strain-rate, mineralogical composition, fluid content, grain size, confining pressure, and temperature (e.g., Bürgmann & Dresen, 2008; Karato, 2010). Using the postseismic anelastic strain inverted by the kinematic joint inversion, we can estimate effective viscosities without making *a priori* assumptions on rheological laws. We estimate the effective transient viscosity of the lower crust after the EMC earthquake using

$$\eta_{\text{eff}} = \frac{\left\| \tau_{\text{b}} + \Delta\tau_0 + \Delta\tau_{\text{post}} \right\|_{\text{II}}}{\left\| \dot{\gamma}_{\text{b}} + \Delta\dot{\gamma}_{\text{post}} \right\|_{\text{II}}} \tag{15}$$

where $\| \ \|_{II}$ indicates the second invariant of deviatoric tensors; τ_{b}, $\Delta\tau_0$, and $\Delta\tau_{\text{post}}$ are the background stress field, coseismic, and postseismic stress change, respectively; $\dot{\gamma}_{\text{b}}$ is the background strain-rate field, and $\Delta\dot{\gamma}_{\text{post}}$ is the strain-rate change during the postseismic period. We compute the coseismic stress change at each volume element by the coseismic slip model from Wei, Fielding, et al. (2011). The postseismic stress changes are computed by the product of stress kernels and anelastic strain changes as described in equation 9. For the postseismic strain-rate change, we take the finite difference of strain versus time in each volume element at targeted epochs following the EMC earthquake.

Background stress and strain-rate levels in the lower crust are challenging to constrain independently. We adopt the method used in the previous studies and evaluate the background strain rate from the relative plate motion distributed over the width of the plate boundary (e.g., Masuti et al., 2016; Moore et al., 2017; Tang et al., 2019). Assuming a relative plate motion of 50 mm/year (DeMets et al., 1990) accommodated over a 300-km-wide region in Southern California, we obtain an average background strain-rate field of about 5×10^{-15}/s, in broad agreement with the observed surface deviatoric strain rate of this region (Kreemer et al., 2012). To estimate the background stress field, we adopt a viscosity of 10^{19} Pa s for the background viscosity in the lower crust, consistent with estimates from previous studies on postseismic deformation (e.g., Hines & Hetland, 2016; Spinler et al., 2015). The background stress level, given by

$$\tau_{\text{b}} = \eta_{\text{b}}\dot{\gamma}_{\text{b}} \tag{16}$$

where η_{b} is the background viscosity, is then estimated at about 0.05 MPa.

We obtain effective viscosities in the lower crust ranging from 10^{18} to 10^{19} Pa s in the first month, with a distinct low-viscosity region correlated with the high heat flow anomaly beneath the Salton Trough (Figure 7a). We find relatively high viscosities in the Peninsular Ranges and the Mojave Desert, which experience a relatively low stress/strain-rate changes following the EMC mainshock. The laterally heterogeneous effective viscosity is compatible with the model results from 18-month observations after the EMC earthquake (Pollitz et al., 2012). We show that neither the different assumptions on background viscosity/strain rate (Figures S11 and S12) nor the assumed depth of afterslip below the Sierra Cucapah-Indiviso fault system (Figure S13) largely affects the spatial pattern of effective viscosity in the first month. These results indicate that the lateral variation of estimated transient viscosity in the lower crust is a robust feature. The effective viscosities in the lower crust gradually converge to the assumed background viscosity after 1 year (Figure 7b), while the region beneath the fault zone hosts the viscosity slightly larger than the background value. This indicates that viscoelastic flow attains strain rates below the long-term average following the postseismic transient, which is necessary to maintain the long-term kinematics of the system.

We do not rule out the lateral variation of the background stress/strain-rate levels, especially in the Salton Trough where the surface strain rate can vary drastically within a relatively short distance (Kreemer et al., 2012). However, the estimated postseismic strain-rate change in the Salton Trough can be an order greater than our assumed background strain rate in the first month. Thus, the effective viscosity estimated by equation 15 is dominated by the transient deformation. In contrast, for the regions that experience low postseismic strain-rate change, the effective viscosity should be close to the background level. This indicates that although our assumption of background strain-rate field is only approximative, it still provides a way to examine the lateral variation of transient viscosity during the postseismic period.

4.5. Temporal Evolution of Lower-Crustal Viscosity

Viscoelastic relaxation can be accommodated by diffusion creep and dislocation creep at steady state, while an initial transient creep is also important for postseismic deformation (e.g., Bürgmann & Dresen, 2008;

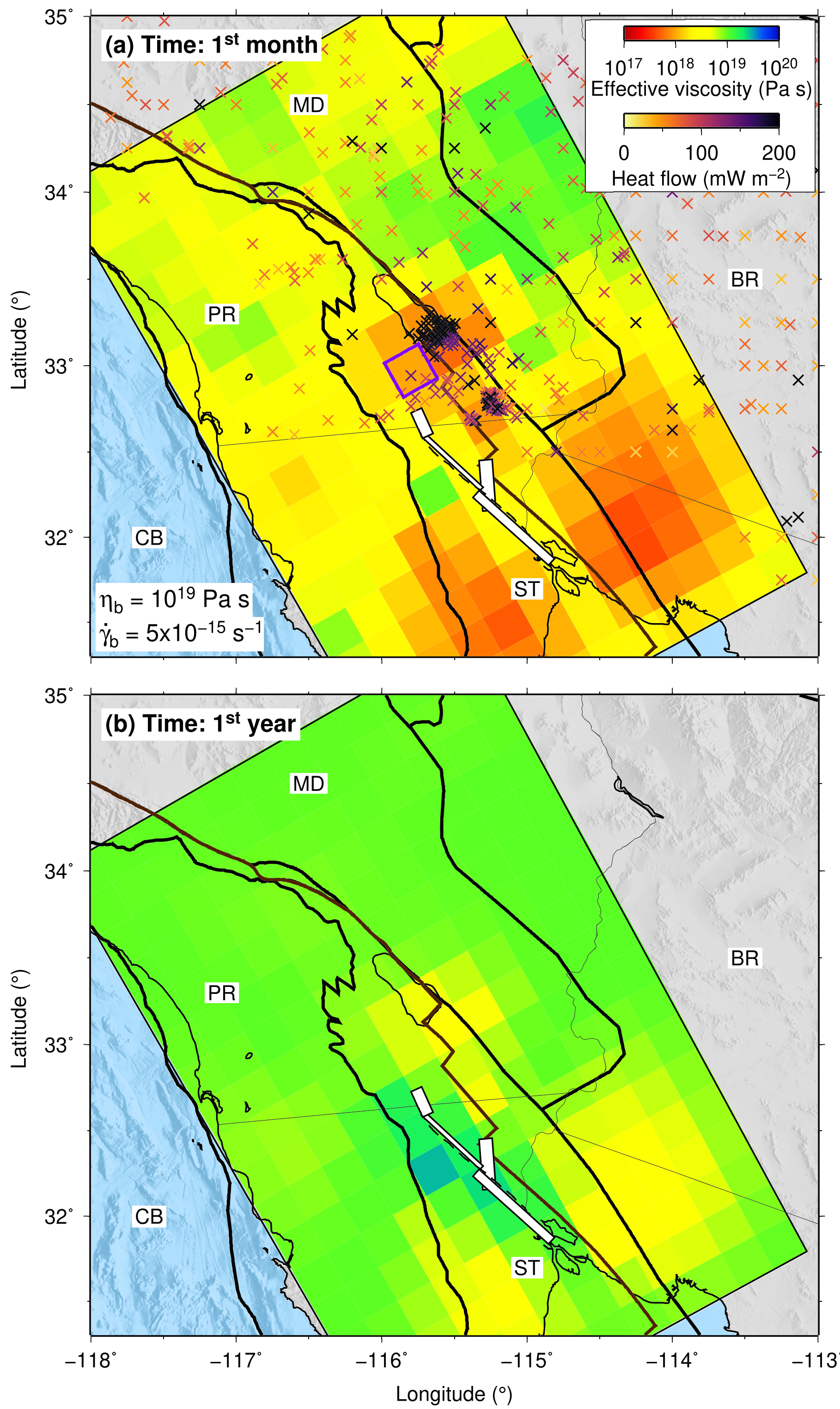

Figure 7. Estimated lower-crustal effective viscosity in (a) the first month and (b) the first year after the EMC earthquake. The unified background viscosity and strain rate are 10^{19} Pa s and about 5×10^{-15}/s, respectively. The purple box marks the volume element beneath the Salton Trough. Black lines enclose the geologic units, and colored crosses mark the observed surface heat flow, as shown in Figure 2.

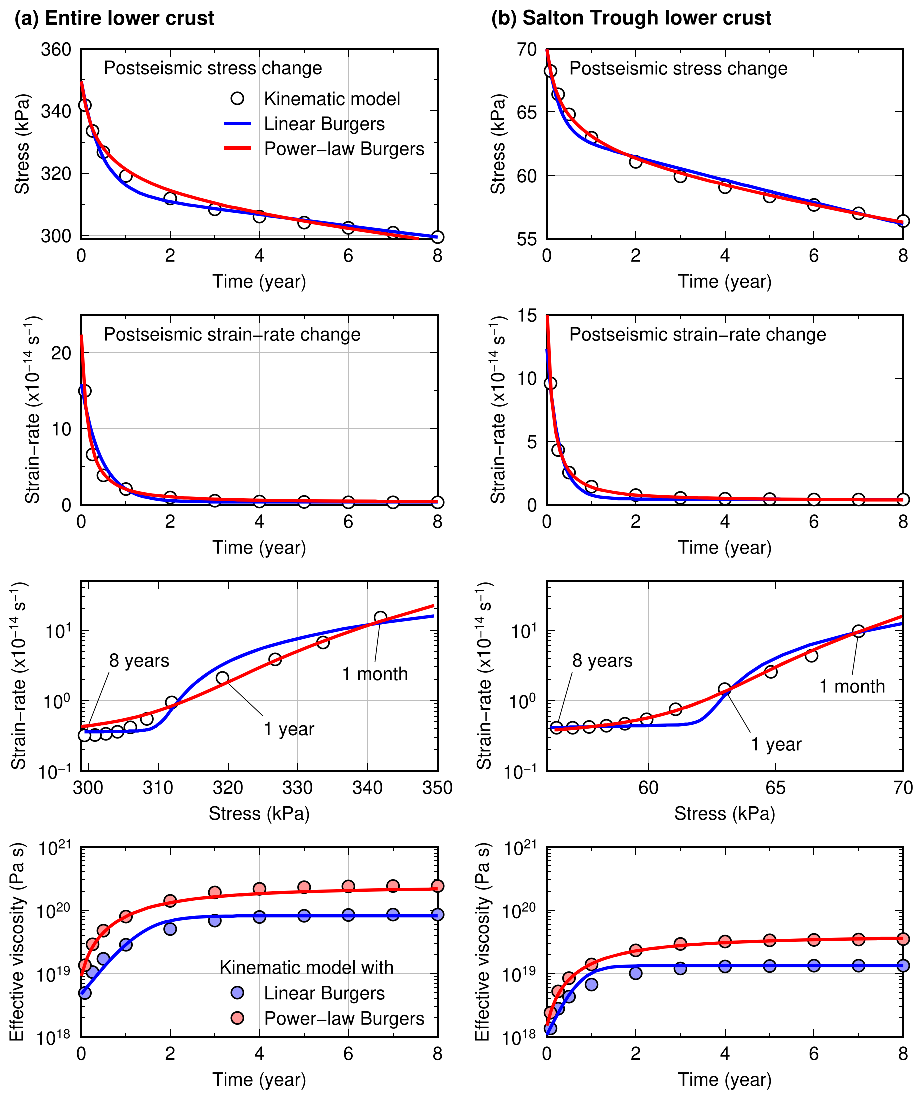

Figure 8. Postseismic stress and strain-rate changes, stress/strain-rate relationship, and effective viscosity evolution in the lower crust approximated by Burgers assemblies with dashpots characterized with either a linear or a power-law rheology (with power of 3). The diagrams show the results of (a) the entire lower crust and (b) the lower crust beneath the Salton Trough (the location is shown in Figure 7a). Stress and strain-rate changes are shown as their second deviatoric invariant with their background values excluded. Note the deviation of the effective viscosities estimated by a linear and power-law rheology due to the different stress exponent.

Wang et al., 2012). A common way to model viscoelastic relaxation with transient creep is using a linear Burgers rheology, which is associated with diffusion creep. However, recent studies have shown that dislocation creep could also play a role in postseismic deformation (e.g., Agata et al., 2019; Freed et al., 2012; Masuti et al., 2016; Muto et al., 2019; Tang et al., 2019; Weiss et al., 2019). To better comprehend the rheological behavior in the lower crust, we adopt the approach from a previous study (Tang et al., 2019) that approximates the viscoelastic deformation using spring-dashpot assemblies to explore the temporal evolution of viscosities and corresponding rheological laws. First, we estimate the evolution of postseismic stress change due to the viscoelastic strain and calculate the finite differences of consecutive postseismic strain-rate change at each epoch. Second, we use spring-dashpot assemblies to simulate the evolution of stress and strain rate. The simulated results are then compared with the stress and strain rate estimated by our kinematic model (Figure 8). This enables us to investigate the constitutive law that governs viscoelastic deformation of rocks in their natural setting, similar to laboratory rock creep experiments but with different spatial and temporal scales.

We employ a Burgers assembly with dashpots characterized with either a linear or a power-law rheology, corresponding to diffusion or dislocation creep, respectively, to test our model results. A Burgers assembly, where a Maxwell element and a Kelvin element are in series, can be described by

$$\dot{\sigma} = -G_{\mathrm{M}}(\dot{\varepsilon}_{\mathrm{M}} + \dot{\varepsilon}_{\mathrm{K}}) \tag{17}$$

where σ is the deviatoric stress, G_{M} is the shear modulus of the Maxwell element, and $\dot{\varepsilon}_{\mathrm{M}}$ and $\dot{\varepsilon}_{\mathrm{K}}$ are the deviatoric strain rate in the Maxwell and Kelvin element, respectively. For a linear Burgers rheology, the dashpots are governed by linear constitutive law, and the governing equations for the deviatoric strain-rate are

$$\dot{\varepsilon}_{\mathrm{M}} = \frac{\sigma}{\eta_{\mathrm{M}}} \tag{18}$$

$$\dot{\varepsilon}_{\mathrm{K}} = \frac{\sigma - 2G_{\mathrm{K}}\varepsilon_{\mathrm{K}}}{\eta_{\mathrm{K}}} \tag{19}$$

where G_{K} is a work-hardening coefficient, ε_{K} is the cumulative strain in the Kelvin element, and η_{M} and η_{K} are the viscosity of dashpot in the Maxwell and Kelvin element, respectively. The product $2G_{\mathrm{K}}\varepsilon_{\mathrm{K}}$ is the internal stress associated with strain partitioning among deformation systems within the mineral. With a power-law Burgers assembly, the governing equations for shear strain rate are

$$\dot{\varepsilon}_{\mathrm{M}} = A_{\mathrm{M}}|\sigma|^{(n_{\mathrm{M}}-1)}\sigma \tag{20}$$

$$\dot{\varepsilon}_{\mathrm{K}} = A_{\mathrm{K}}|\sigma - 2G_{\mathrm{K}}\varepsilon_{\mathrm{K}}|^{(n_{\mathrm{K}}-1)}(\sigma - 2G_{\mathrm{K}}\varepsilon_{\mathrm{K}}) \tag{21}$$

where n_{M} and n_{K} are the stress exponents for the Maxwell and Kelvin elements, respectively, and A_{M} and A_{K} are the respective multiplying factors. For simplicity, we take a stress exponent of $n_{\mathrm{M}} = n_{\mathrm{K}} = 3$, a common value for rocks in the dislocation creep regime. All the parameters used for spring-dashpot assemblies in this study are documented in Table S1.

We first test the averaged stress/strain-rate evolution of the entire lower crust weighted by the magnitude of the deviatoric coseismic stress change in each volume element (Figure 8a). Both linear and power-law Burgers rheology produce a satisfactory fit to the averaged stress and strain-rate time series. However, a power-law Burgers rheology better captures the overall trajectory of strain-rate versus stress, in particular the transition of slopes between the transient and steady-state regimes. The effective viscosities predicted by power-law Burgers rheology are larger than those obtained using linear Burgers rheology due to the different responses of strain rate to stress changes. The estimated transient viscosity for the entire lower crust increases from about 0.5–1 × 10^{19} to 1–2 × 10^{20} Pa s over 8 years following the EMC earthquake.

To examine the lateral heterogeneity of lower-crustal rheology, we use the same approach to test the volume element beneath the Salton Trough (Figure 8b). We again found that a power-law Burgers rheology explains the stress/strain-rate relationship better than a linear Burgers rheology. The estimated effective viscosity beneath the Salton Trough increases from ~10^{18} to 1–4 × 10^{19} Pa s over 8 years, about an order lower than the average effective viscosity in the entire lower crust. The notable difference of the effective viscosity implies the relatively weak lower crust beneath the Salton Trough and the lateral variation of rheology in this region. We apply the same method to test the stress/strain-rate evolution inverted from the deep-fault model described in section 4.2. We find that a power-law Burgers rheology still provides a better fit than a linear one, although the estimated viscosity is higher than in the shallow-fault model (Figure S14). This shows that although the relative contributions of afterslip and viscoelastic flow are different in the two end-member models, the temporal histories of stress/strain rate and their constitutive relationship do not significantly change. Thus, transient rheology and its lateral heterogeneity are still required to explain the data. These results indicate prevailing steady-state dislocation creep following a nonlinear transient creep in the lower crust, similar to the findings from other large earthquakes (e.g., Agata et al., 2019; Masuti et al., 2016; Muto et al., 2019; Tang et al., 2019; Weiss et al., 2019).

In the asthenosphere, we apply the same approach and estimate a transient viscosity from about $1\text{–}2 \times 10^{18}$ to $0.5\text{–}1 \times 10^{19}$ Pa s over 8 years (Figure S15), broadly consistent with previous estimations (e.g., Dickinson-Lovell et al., 2018). However, the deformation at the depth of the asthenosphere is poorly constrained, as discussed in section 4.2, implying a large uncertainty in the inferred effective viscosity. Earthquakes with deep coseismic slip penetrating the entire lithosphere, such as the 2012 Indian Ocean earthquake (Masuti et al., 2016), may be better suited to examine the rheological properties in the asthenosphere. Furthermore, the stress/strain-rate evolution in the lower crust of the Peninsular Ranges and the Mojave Desert cannot be explained by a spring-dashpot assembly. This is likely due to the notable stress interferences induced by the peripheral volume elements, as the coseismic stress change in these regions is relatively low (Figure S16).

5. Conclusions

We show the potential of geodetic observations to probe the constitutive law that governs transient deformation following a large earthquake, extending the framework of rock creep experiments from laboratory to tectonic settings. The 8 years of postseismic deformation following the EMC earthquake can be well explained by localized afterslip and distributed viscoelastic flow with a realistic rheological structure. Viscoelastic flow in the lower crust involves transient creep, nonlinear stress/strain-rate constitutive relationships, and lateral variations of rheological properties. The deformation in the lower crust is compatible with the response of a Burgers assembly, with dashpots following a power-law constitutive law. This implies a marked reduction in effective viscosity following large earthquakes by a combination of the activation of transient creep in the initial postseismic deformation phase and the nonlinear dependence on stress. These findings are compatible with insights from laboratory experiments but provide further constraints on the nonlinear constitutive law that governs transient creep. The effective viscosity in the lower crust of the Salton Trough is about an order of magnitude lower than in the surrounding region. The region of low effective viscosity in the Salton Trough correlates with the thin crust and the large surface heat flow around the trace of the San Andreas fault. These results provide key constraints for the southern section of a California rheology model.

Data Availability Statement

Maps and figures in this study were generated by Generic Mapping Tools (GMT) software package (Wessel et al., 2013) with the topography from the Global Multi-Resolution Topography (GMRT) MapTool (https://www.gmrt.org/GMRTMapTool/). All the GPS time series data in this study can be downloaded from the SOPAC/CSRC GPS Archive (http://garner.ucsd.edu/pub/timeseries/measures/ats/WesternNorthAmerica/).

Acknowledgments

We thank the editor Paul Tregoning, associate editor Michael Poland, and the constructive comments from Takeshi Sagiya and an anonymous reviewer. This study was supported by the National Science Foundation, under award number EAR-1848192, and two Southern California Earthquake Center (SCEC) proposals, under number 18108 and 19100. C.-H. T. and Y.-J. H. was supported by Academia Sinica (AS-CDA-105-M05) and the Ministry of Science and Technology in Taiwan (MOST 104-2628-M-001-008-MY4). This is the contribution of IESAS-2385.

References

Agata, R., Barbot, S. D., Fujita, K., Hyodo, M., Iinuma, T., Nakata, R., et al. (2019). Rapid mantle flow with power-law creep explains deformation after the 2011 Tohoku mega-quake. *Nature Communications*, *10*(1), 1385–1311. https://doi.org/10.1038/s41467-019-08984-7

Barbot, S. (2018a). Asthenosphere flow modulated by Megathrust earthquake cycles. *Geophysical Research Letters*, *45*, 6018–6031. https://doi.org/10.1029/2018GL078197

Barbot, S. (2018b). Deformation of a half-space from Anelastic strain confined in a tetrahedral volume. *Bulletin of the Seismological Society of America*, *108*(5A), 2687–2712. https://doi.org/10.1785/0120180058

Barbot, S., & Fialko, Y. (2010). A unified continuum representation of post-seismic relaxation mechanisms: Semi-analytic models of afterslip, poroelastic rebound and viscoelastic flow. *Geophysical Journal International*, *182*(3), 1124–1140. https://doi.org/10.1111/j.1365-246X.2010.04678.x

Barbot, S., Fialko, Y., & Bock, Y. (2009). Postseismic deformation due to the M_w 6.0 2004 Parkfield earthquake: Stress-driven creep on a fault with spatially variable rate-and-state friction parameters. *Journal of Geophysical Research: Solid Earth*, *114*, B07405. https://doi.org/10.1029/2008JB005748

Barbot, S., Moore, J. D. P., & Lambert, V. (2017). Displacement and stress associated with distributed anelastic deformation in a half-space. *Bulletin of the Seismological Society of America*, *107*(2), 821–855. https://doi.org/10.1785/0120160237

Blackwell, D., & Richards, M. (2004). *Geothermal Map of North America (Scale 1:6,500,000)*. Tulsa, OK: American Association of Petroleum Geologists.

Bruhat, L., Barbot, S., & Avouac, J.-P. (2011). Evidence for postseismic deformation of the lower crust following the 2004 Mw6.0 Parkfield earthquake. *Journal of Geophysical Research: Solid Earth*, *116*, B08401. https://doi.org/10.1029/2010JB008073

Bürgmann, R., & Dresen, G. (2008). Rheology of the lower crust and upper mantle: Evidence from rock mechanics, geodesy, and field observations. *Annual Review of Earth and Planetary Sciences*, *36*(1), 531–567. https://doi.org/10.1146/annurev.earth.36.031207.124326

DeMets, C., Gordon, R. G., Argus, D. F., & Stein, S. (1990). Current plate motions. *Geophysical Journal International*, *101*(2), 425–478. https://doi.org/10.1111/j.1365-246X.1990.tb06579.x

Dickinson-Lovell, H., Huang, M.-H., Freed, A. M., Fielding, E., Bürgmann, R., & Andronicos, C. (2018). Inferred rheological structure and mantle conditions from postseismic deformation following the 2010 Mw 7.2 El Mayor-Cucapah Earthquake. *Geophysical Journal International*, *213*(3), 1720–1730. https://doi.org/10.1093/gji/ggx546

Fletcher, J. M., Teran, O. J., Rockwell, T. K., Oskin, M. E., Hudnut, K. W., Mueller, K. J., et al. (2014). Assembly of a large earthquake from a complex fault system: Surface rupture kinematics of the 4 April 2010 El Mayor–Cucapah (Mexico) Mw 7.2 earthquake. *Geosphere*, *10*(4), 797–827. https://doi.org/10.1130/GES00933.1

Freed, A. M., Hirth, G., & Behn, M. D. (2012). Using short-term postseismic displacements to infer the ambient deformation conditions of the upper mantle. *Journal of Geophysical Research: Solid Earth*, *117*, B01409. https://doi.org/10.1029/2011JB008562

Gonzalez-Ortega, A., Fialko, Y., Sandwell, D., Alejandro Nava-Pichardo, F., Fletcher, J., Gonzalez-Garcia, J., et al. (2014). El Mayor-Cucapah (Mw 7.2) earthquake: Early near-field postseismic deformation from InSAR and GPS observations. *Journal of Geophysical Research: Solid Earth*, *119*, 1482–1497. https://doi.org/10.1002/2013JB010193

Hauksson, E., Stock, J., Hutton, K., Yang, W., Vidal-Villegas, J. A., & Kanamori, H. (2011). The 2010 Mw 7.2 El Mayor-Cucapah Earthquake Sequence, Baja California, Mexico and Southernmost California, USA: Active Seismotectonics along the Mexican Pacific Margin. *Pure and Applied Geophysics*, *168*(8-9), 1255–1277. https://doi.org/10.1007/s00024-010-0209-7

Hines, T. T., & Hetland, E. A. (2016). Rheologic constraints on the upper mantle from 5 years of postseismic deformation following the El Mayor-Cucapah earthquake. *Journal of Geophysical Research: Solid Earth*, *121*, 6809–6827. https://doi.org/10.1002/2016JB013114

Hsu, Y.-J., Simons, M., Avouac, J.-P., Galetzka, J., Sieh, K., Chlieh, M., et al. (2006). Frictional Afterslip following the 2005 Nias-Simeulue Earthquake, Sumatra. *Science*, *312*(5782), 1921–1926. https://doi.org/10.1126/science.1126960

Hu, Y., Bürgmann, R., Freymueller, J. T., Banerjee, P., & Wang, K. (2014). Contributions of poroelastic rebound and a weak volcanic arc to the postseismic deformation of the 2011 Tohoku earthquake. *Earth, Planets and Space*, *66*(1), 106. https://doi.org/10.1186/1880-5981-66-106

Jónsson, S., Segall, P., Pedersen, R., & Björnsson, G. (2003). Post-earthquake ground movements correlated to pore-pressure transients. *Nature*, *424*(6945), 179–183. https://doi.org/10.1038/nature01776

Karato, S. (2010). Rheology of the deep upper mantle and its implications for the preservation of the continental roots: A review. *Tectonophysics*, *481*(1–4), 82–98. https://doi.org/10.1016/j.tecto.2009.04.011

Kreemer, C., Hammond, W., Blewitt, G., Holland, A., & Bennett, R. (2012). A geodetic strain rate model for the Pacific-North American Plate Boundary, western United States. *Nevada Bureau of Mines and Geology Map*, *178*, 6785.

Lambert, V., & Barbot, S. (2016). Contribution of viscoelastic flow in earthquake cycles within the lithosphere-asthenosphere system. *Geophysical Research Letters*, *43*, 10,142–10,154. https://doi.org/10.1002/2016GL070345

Lekic, V., French, S. W., & Fischer, K. M. (2011). Lithospheric thinning beneath rifted regions of Southern California. *Science*, *334*(6057), 783–787. https://doi.org/10.1126/science.1208898

Lillie, R. J. (1999). *Whole Earth Geophysics: An Introductory Textbook for Geologists and Geophysicists* (p. 319). Upper Saddle River, NJ: Prentice Hall.

Loveless, J. P., & Meade, B. J. (2011). Spatial correlation of interseismic coupling and coseismic rupture extent of the 2011 MW = 9.0 Tohoku-oki earthquake. *Geophysical Research Letters*, *38*, L17306. https://doi.org/10.1029/2011GL048561

Masuti, S., Barbot, S. D., Karato, S., Feng, L., & Banerjee, P. (2016). Upper-mantle water stratification inferred from observations of the 2012 Indian Ocean earthquake. *Nature*, *538*(7625), 373–377. https://doi.org/10.1038/nature19783

Mickus, K., & Hussein, M. (2016). Curie depth analysis of the Salton Sea Region, Southern California. *Pure and Applied Geophysics*, *173*(2), 537–554. https://doi.org/10.1007/s00024-015-1100-3

Moore, J. D. P., Yu, H., Tang, C.-H., Wang, T., Barbot, S., Peng, D., et al. (2017). Imaging the distribution of transient viscosity after the 2016 M_w 7.1 Kumamoto earthquake. *Science*, *356*, 163–167. https://doi.org/10.1126/science.aal3422

Muto, J., Moore, J. D. P., Barbot, S., Iinuma, T., Ohta, Y., & Iwamori, H. (2019). Coupled afterslip and transient mantle flow after the 2011 Tohoku earthquake. *Science Advances*, *5*, eaaw1164. https://doi.org/10.1126/sciadv.aaw1164

Okada, Y. (1985). Surface deformation due to shear and tensile faults in a half-space. *Bulletin of the Seismological Society of America*, *75*, 1135–1154.

Okada, Y. (1992). Internal deformation due to shear and tensile faults in a half-space. *Bulletin of the Seismological Society of America*, *82*, 1018–1040.

Pollitz, F. F., Bürgmann, R., & Thatcher, W. (2012). Illumination of rheological mantle heterogeneity by the M7.2 2010 El Mayor-Cucapah earthquake. *Geochemistry, Geophysics, Geosystems*, *13*, Q06002. https://doi.org/10.1029/2012GC004139

Qiu, Q., Moore, J. D. P., Barbot, S., Feng, L., & Hill, E. M. (2018). Transient rheology of the Sumatran mantle wedge revealed by a decade of great earthquakes. *Nature Communications*, *9*(1), 995. https://doi.org/10.1038/s41467-018-03298-6

Rollins, C., Barbot, S., & Avouac, J.-P. (2015). Postseismic deformation following the 2010 M = 7.2 El Mayor-Cucapah earthquake: Observations, kinematic inversions, and dynamic models. *Pure and Applied Geophysics*, *172*, 1305–1358. https://doi.org/10.1007/s00024-014-1005-6

Spinler, J. C., Bennett, R. A., Walls, C., Lawrence, S., & García, J. J. G. (2015). Assessing long-term postseismic deformation following the M7.2 4 April 2010, El Mayor-Cucapah earthquake with implications for lithospheric rheology in the Salton Trough. *Journal of Geophysical Research: Solid Earth*, *120*, 3664–3679. https://doi.org/10.1002/2014JB011613

Tang, C.-H., Hsu, Y.-J., Barbot, S., Moore, J. D. P., & Chang, W.-L. (2019). Lower-crustal rheology and thermal gradient in the Taiwan orogenic belt illuminated by the 1999 Chi-Chi earthquake. *Science Advances*, *5*, eaav3287. https://doi.org/10.1126/sciadv.aav3287

Tape, C., Plesch, A., Shaw, J. H., & Gilbert, H. (2012). Estimating a continuous Moho surface for the California unified velocity model. *Seismological Research Letters*, *83*(4), 728–735. https://doi.org/10.1785/0220110118

Thatcher, W. R., Hearn, E. H., Oskin, M. E., Montesi, L. G., Hirth, G., Behr, W. M., et al. (2019, September). Preliminary SCEC Community Rheology Model. Poster #317 presented at the 2019 SCEC Annual Meeting, Palm Springs CA. Retrieved from https://www.scec.org/publication/9833

Tsang, L. L. H., Hill, E. M., Barbot, S., Qiu, Q., Feng, L., Hermawan, I., et al. (2016). Afterslip following the 2007 M_w 8.4 Bengkulu earthquake in Sumatra loaded the 2010 M_w 7.8 Mentawai tsunami earthquake rupture zone. *Journal of Geophysical Research: Solid Earth*, *121*, 9034–9049. https://doi.org/10.1002/2016JB013432

Wang, K., Hu, Y., & He, J. (2012). Deformation cycles of subduction earthquakes in a viscoelastic Earth. *Nature*, *484*(7394), 327–332. https://doi.org/10.1038/nature11032

Wei, M., Sandwell, D., Fialko, Y., & Bilham, R. (2011). Slip on faults in the Imperial Valley triggered by the 4 April 2010 Mw 7.2 El Mayor-Cucapah earthquake revealed by InSAR. *Geophysical Research Letters*, *38*, L045235. https://doi.org/10.1029/2010GL045235

Wei, S., Fielding, E., Leprince, S., Sladen, A., Avouac, J.-P., Helmberger, D., et al. (2011). Superficial simplicity of the 2010 El Mayor–Cucapah earthquake of Baja California in Mexico. *Nature Geoscience*, *4*(9), 615–618. https://doi.org/10.1038/ngeo1213

Weiss, J. R., Qiu, Q., Barbot, S., Wright, T. J., Foster, J. H., Saunders, A., et al. (2019). Illuminating subduction zone rheological properties in the wake of a giant earthquake. *Science Advances*, *5*, eaax6720. https://doi.org/10.1126/sciadv.aax6720

Wessel, P., Smith, W. H. F., Scharroo, R., Luis, J., & Wobbe, F. (2013). Generic mapping tools: Improved version released. *Eos, Transactions American Geophysical Union*, *94*(45), 409–410. https://doi.org/10.1002/2013EO450001